Mechanical resilience and cementitious processes in Imperial Roman architectural mortar

Article *in* Proceedings of the National Academy of Sciences · December 2014

DOI: 10.1073/pnas.1417456111

10 authors, including:

Marie Jackson
University of Utah
69 PUBLICATIONS **2,114** CITATIONS
SEE PROFILE

Eric N. Landis
University of Maine
119 PUBLICATIONS **4,205** CITATIONS
SEE PROFILE

Philip Brune
Magic Leap
11 PUBLICATIONS **281** CITATIONS
SEE PROFILE

Massimo Vitti
Sovrintendenza Beni Culturali Roma Capitale
14 PUBLICATIONS **202** CITATIONS
SEE PROFILE

Mechanical resilience and cementitious processes in Imperial Roman architectural mortar

Marie D. Jackson[a,1], Eric N. Landis[b], Philip F. Brune[c], Massimo Vitti[d], Heng Chen[a,e], Qinfei Li[a,f], Martin Kunz[g], Hans-Rudolf Wenk[h], Paulo J. M. Monteiro[a], and Anthony R. Ingraffea[i]

Departments of [a]Civil and Environmental Engineering and [h]Earth and Planetary Science, University of California, Berkeley, CA 94720; [b]Department of Civil and Environmental Engineering, University of Maine, Orono, ME 04469; [c]DuPont Engineering Research & Technology, Wilmington, DE 19805; [d]Sovrintendenza Capitolina Beni Culturali di Roma Capitale, Ufficio Fori Imperiali, Rome 00187, Italy; [g]Lawrence Berkeley National Laboratory, Berkeley, CA 94720; [i]Department of Civil and Environmental Engineering, Cornell University, Ithaca, NY 14853; [e]School of Materials Science and Engineering, Southeast University, Nanjing 211189, China; and [f]School of Transportation Science and Engineering, Harbin Institute of Technology, Harbin, Heilongjiang 150090, China

Edited by David J. Killick, University of Arizona, and accepted by the Editorial Board October 27, 2014 (received for review September 12, 2014)

The pyroclastic aggregate concrete of Trajan's Markets (110 CE), now Museo Fori Imperiali in Rome, has absorbed energy from seismic ground shaking and long-term foundation settlement for nearly two millenia while remaining largely intact at the structural scale. The scientific basis of this exceptional service record is explored through computed tomography of fracture surfaces and synchroton X-ray microdiffraction analyses of a reproduction of the standardized hydrated lime–volcanic ash mortar that binds decimeter-sized tuff and brick aggregate in the conglomeratic concrete. The mortar reproduction gains fracture toughness over 180 d through progressive coalescence of calcium–aluminum-silicate–hydrate (C-A-S-H) cementing binder with Ca/(Si+Al) ≈ 0.8–0.9 and crystallization of strätlingite and siliceous hydrogarnet (katoite) at ≥90 d, after pozzolanic consumption of hydrated lime was complete. Platey strätlingite crystals toughen interfacial zones along scoria perimeters and impede macroscale propagation of crack segments. In the 1,900-y-old mortar, C-A-S-H has low Ca/(Si+Al) ≈ 0.45–0.75. Dense clusters of 2- to 30-μm strätlingite plates further reinforce interfacial zones, the weakest link of modern cement-based concrete, and the cementitious matrix. These crystals formed during long-term autogeneous reaction of dissolved calcite from lime and the alkali-rich scoriae groundmass, clay mineral (halloysite), and zeolite (phillipsite and chabazite) surface textures from the Pozzolane Rosse pyroclastic flow, erupted from the nearby Alban Hills volcano. The clast-supported conglomeratic fabric of the concrete presents further resistance to fracture propagation at the structural scale.

Roman concrete | volcanic ash mortar | fracture toughness | interfacial zone | strätlingite

The builders of the monuments of Imperial Rome (from 27 BCE, when Octavian became Emperor Augustus, through the fourth century CE) used pyroclastic volcanic rock to create unreinforced concrete structures with dramatic vaulted spans, as at the Markets of Trajan (110 CE) (1, 2) (Fig. 1*A*). The concrete foundations, walls, and vaulted ceilings are composed of decimeter-sized volcanic tuff and brick coarse aggregate (*caementa*) bound by volcanic ash–lime mortar (Fig. 1*B*). The conglomeratic fabric of the concretes is analogous to sedimentary rocks made of coarse rock fragments and a matrix of finer grained material. The concretes have resisted structural scale failure during moderate-magnitude earthquakes (<8 on the Mercalli–Cancani–Sieberg intensity scale) associated with slip on Appennine fault systems 80–130 km to the northeast, as well as chemical decay associated with repeated inundations of foundations and walls by Tiber River floods (3–5). To date, at least six episodes of moment magnitude 6.7–7 ground shaking and damage to monuments have been recorded since 508 CE (4). The concrete structures contain common macroscale fractures, with rough surfaces that link by complex segment overlap and bridging, and either follow or traverse *caementa* interfacial zones (Fig. 1*C*). Many monuments remain in active use as residences, offices, museums, and churches. In addition to the Markets of Trajan, these include the Theater of Marcellus (44–13 BCE), Mausoleum of Hadrian (123–39 CE), Pantheon (*ca.* 126 CE), and Baths of Diocletian (298–306 CE). The monuments that did undergo sectional failure, for example at the Colosseum (70–90 CE), Baths of Caracalla (*ca.* 215 CE), and Basilica of Maxentius (*ca.* 313 CE), mainly did so in Late Antiguity or the Middle Ages, when they were several centuries old and had become vulnerable through subsurface instabilities; problematic structural design; removal of marble and travertine dimension stone, columns, and cladding; and lack of regular maintenance (4, 6, 7).

The pozzolanic mortar perfected by Roman builders during first century BCE (8) is key to the durability of concrete components in structurally sound monuments well maintained over two millennia of use. [Pozzolans, named after pumiceous ash from Puteoli (now, Pozzuoli) in the Campi Flegrei volcanic district, react with lime in the presence of moisture to form binding cementitious hydrates (9)]. By the Augustan era (27 BCE–14 CE), after experimenting with ash mixtures for >100 y, Romans had a standardized mortar formulation using scoriaceous ash of the mid-Pleistocene Pozzolane Rosse pyroclastic flow (Fig. S1) that substantially improved the margin of safety associated with increasingly daring structural designs (10, 11). They used this mortar formulation in the principal Imperial monuments constructed in Rome through early fourth century CE (8). Pozzolane Rosse erupted at 456 ± 3 ka from nearby Alban Hills volcano

Significance

A volcanic ash–lime mortar has been regarded for centuries as the principal material constituent that provides long-term durability to ancient Roman architectural concrete. A reproduction of Imperial-age mortar based on Trajan's Markets (110 CE) wall concrete resists microcracking through cohesion of calcium–aluminum–silicate–hydrate cementing binder and in situ crystallization of platey strätlingite, a durable calcium-aluminosilicate mineral that reinforces interfacial zones and the cementitious matrix. In the 1,900-y-old mortar dense intergrowths of the platey crystals obstruct crack propagation and preserve cohesion at the micron scale. Trajanic concrete provides a proven prototype for environmentally friendly conglomeratic concretes that contain ∼88 vol % volcanic rock yet maintain their chemical resilience and structural integrity in seismically active environments at the millenial scale.

Author contributions: M.D.J., E.N.L., P.F.B., M.V., H.-R.W., P.J.M.M., and A.R.I. designed research; M.D.J., E.N.L., P.F.B., M.V., M.K., H.-R.W., and A.R.I. performed research; M.D.J., E.N.L., P.F.B., H.C., Q.L., M.K., and A.R.I. analyzed data; and M.D.J., E.N.L., and P.F.B. wrote the paper.

The authors declare no conflict of interest.

This article is a PNAS Direct Submission. D.J.K. is a guest editor invited by the Editorial Board.

Freely available online through the PNAS open access option.

[1]To whom correspondence should be addressed. Email: mdjjackson@gmail.com.

This article contains supporting information online at www.pnas.org/lookup/suppl/doi:10.1073/pnas.1417456111/-/DCSupplemental.

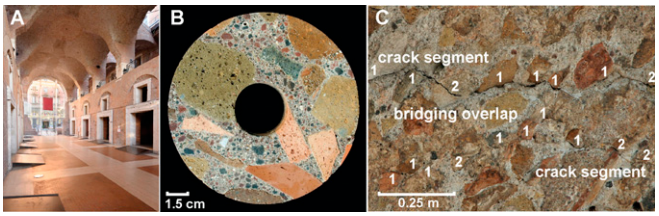

Fig. 1. Markets of Trajan concretes. (*A*) Great Hall, vaulted ceiling and brick-faced concrete walls; reprinted with permission from Archives, Museo Fori Imperiali. (*B*) Drill core with Pozzolane Rosse volcanic ash (*harena fossicia*) mortar and conglomeratic aggregate (*caementa*). (*C*) Fractures in vaulted ceiling, *Grande Emiciclo*: 1, crack follows *caementa* perimeter; 2, crack traverses *caementa*. Wall concrete contains ~88 vol % pyroclastic rock: 45–55% tuff (and brick) as *caementa*, ~38% volcanic ash pozzolan, and ~12% lime paste, with 3:1 ash:lime volumetric ratio (*de Architectura* 2.5.1) in the mortar (18).

(12), filling valleys and covering topographic plateaus across the Roman region; the ash has a highly potassic tephritic composition (13). Romans made the architectural mortars by calcining limestone at ~900 °C to produce quicklime [CaO], hydrating the quicklime to form portlandite [$Ca(OH)_2$], a trigonal calcium hydroxide] putty, and laboriously incorporating granular Pozzolane Rosse ash. This is the red and black excavated sand (*harena fossicia*) described by the Roman architect Vitruvius in first century BCE (*de Architectura* 2.4.1–2.4.3; 2.5.1–2.5.3) (14). The strongly alkaline portlandite solution attacks the surfaces of the scoriaceous pozzolan; volcanic glass and silicate mineral textures dissociate; their alkali ions dissolve in the liquid phase; and calcium is adsorbed on the scoria surfaces, forming cementitious hydrates (9). These phases are regarded as central to the chemical durability that is an essential component of the impressive record of survival of many monuments, but their role in resisting mechanical degradation through obstructing microcrack propagation has never been examined.

Fracture-mechanical properties offer important insight into a cementitious material's long-term survivability (i.e., its ability to absorb energy from applied loads without failing catastrophically). Two common properties are uniaxial tensile strength [f_t (megapascals)], which refers to the stress at which a macrocrack initiates, and fracture energy [G_F (joules per square meter)], the amount of mechanical work required to propagate a macrocrack to create one square unit of new surface area (15). Experimental characterization of the fracture behavior of the Imperial-age mortar through tests of ancient material is difficult, because it occurs in narrow, irregular zones that are bonded to *caementa* (Fig. 1*B*), and the heterogeneous fabric of the concrete requires large test dimensions (16). We therefore duplicated the Imperial-age mortar using the volcanic ash–quicklime proportions described by Vitruvius (*de Architectura* 2.4–2.5) (14) and petrographic and mineralogical characterization of mortar samples from the Great Hall of Trajan's Markets (17) to formulate a mix design that closely mimics the Trajanic formulation. Fracture-mechanical properties, as well as Young's modulus, were previously determined at 28, 90, and 180 d hydration via an innovative arc-shaped three-point bending test (18) that reproduced half-slices of hollow 20-cm-diameter drill cores from the Great Hall (Fig. 1*B*), so that the behavior of the mortar reproduction can be compared with that of Trajanic concrete in a future experimental testing program. All measured properties increase with age, with the 180-d mortar producing values for Young's modulus and uniaxial tensile strength around 1/10 of modern structural concrete, whereas fracture energy is close to one-half (Table 1). We now seek to explain this relatively tough behavior and its evolution with age using SEM imaging, X-ray microdiffraction analyses, and fracture tomography to provide insight into the measured experimental responses and the multiscale processes that contribute to the extraordinary chemical and mechanical durability of the large concrete elements of the Roman monuments. Computed X-ray tomographic studies (Fig. S2) of the crack arrays in the reproduction at 28, 90, and 180 d hydration provide visualization of millimeter-scale fracture processes to which macroscale toughness associated with previously published G_F values are attributed (18). X-ray microdiffraction experiments with synchroton radiation are a critical analytic component, because they provide very fine-scale identifications of the cementitious mineral assemblage that evolved over 1,900 y. The Markets of Trajan concrete provides a proven prototype for innovations in monolithic concretes (19) that are reinforced by a clast-supported conglomeratic fabric at the macroscale and an enduring crystalline fabric at the microscale. New concrete materials formulated with pyroclastic aggregate based on the Imperial Roman prototype could reduce carbon emissions, produce crystalline cementitious reinforcements over long periods of time, enhance durability in seismically active regions, and extend the service life of environmentally sustainable buildings.

Trajanic Mortar Reproduction

The Imperial-age architectural mortar formulation is a deceptively simple mix of volcanic ash and lime. Pozzolane Rosse ash contains illuvial surface coatings of poorly crystalline clay (halloysite) and opal in an upper pedogenic horizon and zeolitic surface coatings (phillipsite and chabazite) in a lower horizon altered in ground water (8). These natural mineral cements have excellent pozzolanic properties (9). Relicts of these textures survive in scoriae in Trajanic mortar, and the relative proportions of the pedogenic and zeolitic alteration facies determined through petrographic studies (8, 17) were replicated in the mortar reproduction. The volcanic ash mix thus contains Pozzolane Rosse ash from the reddened intermediate alteration facies at Fossignano and Castel di Leva quarries and the dark-gray lower alteration facies of Corcolle quarry, sieved in the grain size distribution at Castel di Leva quarry (Fig. S1 and Table S1). The mix includes 5 wt % finely ground, zeolitized Tufo Lionato tuff, because this is observed in certain Trajanic mortars.

The poorly crystalline cementing binder of the mortar is calcium–aluminum–silicate–hydrate (C-A-S-H) (Fig. 2). This is the principal cementitious component of environmentally friendly concretes that partially replace Portland cement with alumino-silicate supplemental materials to reduce CO_2 emissions associated with cement manufacture and improve chemical durability, at least at the decadal time scale (20, 21). X-ray powder and microdiffraction (Fig. 3 and Fig. S3) detect the fine-grained cementitious mineral phases that crystallized in situ: hydrotalcite $Mg_6Al_2(OH)_{16}[CO_3]\cdot 4H_2O$, a trigonal, double-layered carbonate (22), reflects Mg^{2+} dissolved

Table 1. Mechanical properties of mortar reproductions

Measurement	Age of mortar, d		
	28	90	180
Trajanic mortar reproduction, inverse FEA analysis*			
Work of fracture, N/mm	66	675	886
Fracture energy (G_F), J/m^2	5	45	55
Young's modulus (E), GPa	1.00	2.90	3.37
Tensile strength (F_c), MPa	0.08	0.47	0.55
Modulus of rupture (R), MPa	0.19	1.02	1.32
Trajanic mortar reproduction, tomographic analysis†			
Traced crack area, mm^2	22,332	13,596	17,746
Fracture energy (G_f), J/m^2	3	52	50
Roman architectural mortar replica‡			
Young's modulus (E), GPa	3.43	2.96	3.24
Modulus of rupture (R), MPa	1.31	1.35	1.09
Compressive strength (F_c), MPa	9.68	13.32	13.04

*From ref. 18.
†Table S2.
‡From ref. 16.

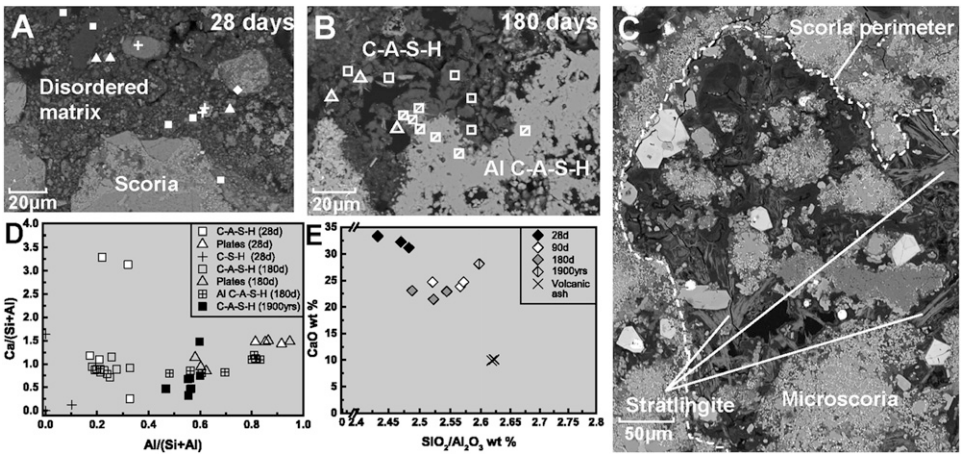

Fig. 2. Cementitious components, SEM-BSE images, and compositional analyses. (*A*) Cementitious matrix at 28 d. (*B*) Cementitious matrix at 180 d. (*C*) Great Hall mortar, interfacial zone along scoria perimeter. (*D*) SEM-EDS analyses of *A* and *B*, Ca/(Si+Al) vs. Al/(Si+Al) as atomic percent ratios of total Ca+Si+Al+Na^{+}K+Mg+Fe+Ti (Table S4). (*E*) bulk composition of cementitious matrix (<74-μm powder) as weight percent oxides (Table S5).

from scoriae, which contain about 3–4 wt % MgO (8); strätlingite [gehlenite hydrate, $Ca_2Al(AlSi)O_2(OH)_{10}{\cdot}2.25H_2O$], a trigonal phyllosilicate with perfect cleavage parallel (0001) and a 12.5-Å d-spacing basal layer (23); katoite [$Ca_3Al_2(SiO_4)_{1.5}(OH)$], a cubic, siliceous hydrogarnet in the nesosilicate hydrogrossular solid solution series (24); and åkermanite [$Ca_2Mg(Si_2O_7)$], a magnesium sorosilicate of the melilite group, in solid solution with gehlenite [$Ca_2Al_2(SiO_7)$] (25). These minerals occur in concretes that partially replace Portland cement with blast-furnace slag (26), metakaolinite (27), and zeolite (28). Strätlingite, katoite, gehlenite, and åkermanite crystallize as stable rock-forming minerals in altered, alkaline-rich, Pliocene–Pleistocene lavas north of Rome (29).

The large increase in peak load and fracture energy between 28 and 90 d (Fig. 4 *E* and *F*) is the result of changes in crack interactions with the evolving cementitious matrix (Fig. 2). Mapping of fracture surfaces on computed tomographic scans to record crack tortuosity, segmentation, and microstructural features at the millimeter scale (Fig. 4 *A–D* and Fig. S2) show that 28-d specimens have larger crack areas than the 90- and 180-d specimens (Table 1 and Table S2). The cracks mainly propagated through the highly disordered matrix, which is poorly bonded to the scoriaeous pozzolan (Fig. 2*A*). They follow the weakest path around sand- and gravel-sized scoriae (Fig. 4 *A* and *C*). The result is a low G_F of 5 J/m^2 (Fig. 4*F*) (18). The cracks propagating through the 90- and 180-d specimens are locally less rough and composed of *en echelon* crack segments (Fig. 4 *B* and *D*). Sand- and gravel-sized scoriae obstruct crack growth at the millimeter scale, causing crack deflection and segment offsets that increase overall toughness. These indicate a more cohesive cementitious matrix that is firmly bonded to scoria. Fracture propagation consumed more energy, yielding G_F values of 45 and 55 J/m^2, respectively (Fig. 4*F*) (18), yet the loss of load-carrying capacity (Fig. 4*E*) occurred through a crack array that has lower surface area than that of the 28-d specimens. When the mapped tomographic crack surface area (square meters) is normalized by the measured work of fracture (joules), the experimental measure of fracture energy (G_f) agrees well with previously published values (Fig. 4*F* and Table 1). The microstructural origins of fracture toughening mechanisms at >90 d are associated with coalescence of C-A-S-H into >100-$μm^2$ areas,

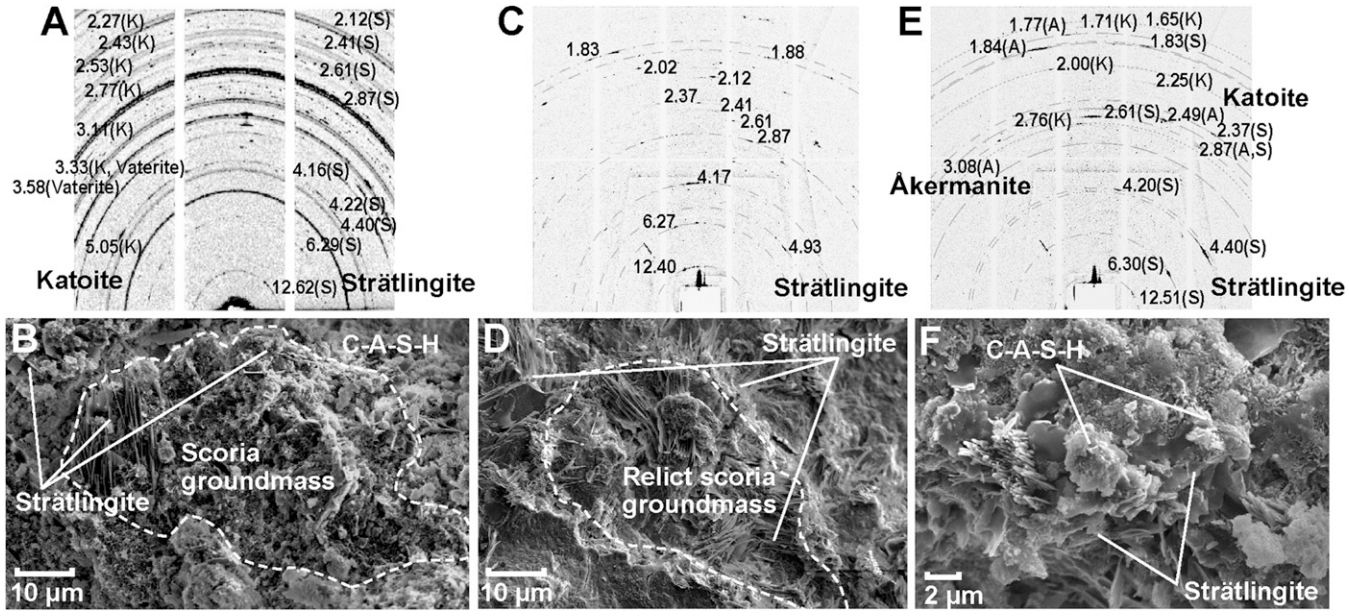

Fig. 3. X-ray microdiffraction analysis (Debye diffraction rings, Table S3) and SEM-secondary electron images. (*A* and *B*) cementitious matrix and scoria perimeter at 180 d. (*C* and *D*) Trajan's Market foundation, relict scoria. (*E* and *F*) Trajan's Market foundation, cementitious matrix. Debye ring traces of higher-intensity d-spacings of coarse-grained crystals (*C* and *E*). Short dashes, katoite; dots and dashes, strätlingite; long dashes, åkermanite.

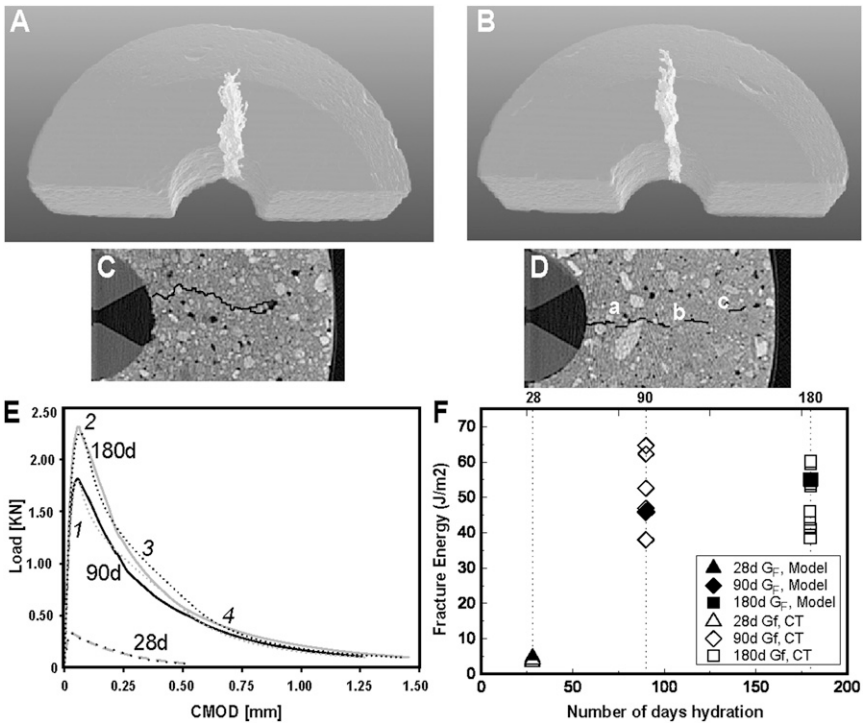

Fig. 4. Fracture testing of the wall mortar reproduction. (*A* and *B*) Tomographic studies of 28- and 180-d specimens. (*C* and *D*) Axial zone tomographic slices at 28 and 180 d. a, b, and c are crack segments. (*E*) experimental (solid) and computational (dashed) results of load-CMOD curves (18): region (*1*) before the curve reaches its peak (*2*) signals growth of microcracks, a smooth postpeak descent (*3*) indicates stable growth of a critical macrocrack and weakening of the specimen (*4*), similar to fracture of quasi-brittle materials (30) in present-day concrete (31, 32). Reprinted from ref. 18. (*F*) Fracture energy (G_f) measured from mapped fractures compared with G_F previously determined through FEA (18) (Table S2).

disappearance of portlandite, and crystallization of strätlingite and katoite (Fig. S3), similar to environmentally friendly slag concretes (20). At 180 d, very fine-grained (<1 μm) strätlingite and katoite in the cementitious matrix produce continuous Debye ring patterns determined through X-ray microdiffraction (Fig. 3*A* and Table S3); strätlingite (2–5 μm) also occurs along the perimeter of mainly intact scoriae (Fig. 3*B*). Although G_F is about one-half that of cement mortar and geopolymer concrete with comparable aggregate sizes (15, 33), long-term C-A-S-H coalescence and strätlingite crystallization likely produce higher toughness in the Trajanic mortar (Figs. 2*C* and 3 *C*–*F*).

Development of the Cementitious Fabric

At 28 d of hydration, the cementitious matrix is a disordered composite of partially reacted microscoria, clinopyroxene, leucite, and analcime crystal fragments, and opal from the volcanic ash; relict portlandite; and irregular patches (<50 μm) of C-A-S-H binder with variable composition, calcium-aluminosilicate fibers (<10 μm), and hydrotalcite crystals (Fig. 2 *A* and *D* and Fig. S3). The heterogeneous C-A-S-H compositions likely reflect availability of Al^{3+} and Si^{4+} at gel nucleation sites (34, 35), as suggested by formation of calcium–silicate–hydrate (C-S-H) adjacent to relict opal particles and alumina-enriched C-A-S-H adjacent to scoriae perimeters (Table S4). By 90 d, when portlandite is entirely consumed (Fig. S3), areas of C-A-S-H binder further coalesce, similar to fresh geopolymer pastes (36), and katoite and strätlingite crystals appear. At 180 d of hydration, C-A-S-H binder with Ca/(Si+Al) ≈ 0.8–0.9 occurs in larger zones (≤200 μm), and C-A-S-H is further enriched in aluminum along scoria perimeters (Fig. 2 *B* and *D*). The high calcium content of the fine fraction of the 28-d cementitious matrix, 32 wt % CaO, decreases to 22 wt % at 90 and 180 d of hydration. The composition becomes more siliceous, as well, similar to the ancient matrix in the foundation of Trajan's Markets (Fig. 2*E* and Table S5). There, C-A-S-H binder with low Ca/(Si+Al) ≈ 0.45–0.75 (Fig. 2 *C* and *D*) may enhance chemical stability, through irreversible binding of alkali cations [Na_2O+K_2O is ~1.5 wt % (Table S5)] and mitigation of damaging alkali silica reactions (37), even after repeated saturation with floodwaters. Dense intergrowths of coarse strätlingite ≤30 μm, with aspect ratios ranging from 3:1 laths to curving 1:1 plates, occupy scoria interfacial transition zones; the groundmass of silt-sized scoriae is nearly wholly replaced by strätlingite (Fig. 3 *C* and *D*). In the cementitious matrix, coarse 2- to 5-μm crystals of strätlingite, katoite, and åkermanite produce discontinuous Debye ring patterns (Fig. 3 *E* and *F*); åkermanite could reflect long-term transformation of hydrotalcite to a more stable silicate phase (38). The close similarity between the cementitious microstructures and mineral assemblage of the 180-d reproduction and the Trajanic mortar indicates that the reformulation is a good match for that developed by Roman builders.

Role of Pyroclastic Rock in Concrete Durability

The strätlingite crystals in Imperial Roman mortar resemble microfibers that are added to the cement paste of present-day mortars and concretes to produce toughening—except that they crystallized in situ and reinforce interfacial zones, the most vulnerable component of the mortar fabric (39–41). The crystals show no corrosion: Their smooth (0001) surfaces indicate long-term stability, similar to strätlingite that persists in the geological record for hundreds of thousands of years (23). Laboratory syntheses of strätlingite in cement pastes at ambient temperatures are accelerated by alkali activators, principally sodium silicate solution or zeolite particles (26–28). Dissolution of alkali-rich Pozzolane Rosse volcanic glass and natural halloysite and zeolite textures in microscoriae accretions along scoria perimeters (8) produced high concentrations of alkali cations and a favorable environment for strätlingite crystallization (Fig. 2*C*). The complex accretionary ash microstructures obstruct debonding of scoriae, not necessarily through the interfacial densification process noted for cement pastes with blast-furnace slag, silica fume, and limestone admixtures (26, 42–44), but rather through interconnectivity of dense bundles of strätlingite plates among microscoriae that attach to irregular scoria surfaces and the cementitious matrix.

In Portland cement mortars and concretes, crack paths preferentially develop in the porous interfacial zone between the fine-grained cement paste and largely inert sand and gravel aggregate (39, 45). Macrofibers and microfibers mixed in cement paste provide obstacles to crack propagation; toughening is produced by the initiation of multiple microcracks developed

through strain-hardening processes, segment offsets, and crack bridging (40). The wider dispersion of cracks causes a load redistribution, so that additional energy is absorbed by a diffuse network of microcracks rather than a single localized macrocrack (46). Although strätlingite crystals have relatively low bulk modulus [about 23 GPa, compared with 34 GPa for C-A-S-H with Ca/(Si+Al) = 0.72 in slag concrete (47, 48)] they evidently play a role in impeding the propagation of microcracks in Roman architectural mortar, similar to polypropylene microfibers with low elastic modulus interground with cement in present-day mortars (40). Three principal differences exist between authigenic strätlingite crystals in Roman mortar and microfiber additives in present-day cement pastes. First, radial spherulites of strätlingite grow preferentially in scoria interfacial zones (Figs. 2*C* and 3*D*), whereas microfiber additives remain in the cement paste and do not reinforce aggregate interfacial zones. Second, strätlingite is resistant to corrosion (24), relative to glass and steel fibers in cement matrices (49). Third, authigenic crystallization of dense strätlingite intergrowths occurs in the complex accretionary perimetral zones of scoriae (Fig. 2*C*), groundmass of scoriae (Fig. 3*D*), and cementitious matrix (Fig. 3*F*) long after portlandite was consumed at about 90 d of hydration (Table S3). This latent crystallization reflects dissolution of volcanic glass with ∼10 wt % CaO (Fig. 2*E* and Table S5) and relict lime clasts composed of calcite and long-term reaction with pore fluids in the Trajanic concrete. A similar process of strätlingite crystallization occurs in calcic inclusions in alkali-rich lavas near Rome (23, 29).

Modern concrete mixtures contain a large proportion of very reactive and finely ground cement that hydrates quickly and develops high early strength and modulus of elasticity, but also high autogeneous temperature rise. Shrinkage strains develop through thermal drying, exudation, and volume change in the 10- to 50-μm interfacial transition layer between cement paste and aggregates; these induce tensile stress and an immeasurable number of minor cracks. As microcracks interconnect and form macrocracks, ingress of water and aggressive ions is enhanced, expansive deterioration processes are accelerated, and premature structural deterioration occurs from corrosion of steel reinforcement, freezing and thawing cycles, and alkali-aggregate reaction (19, 43, 50). When strength gain is slow and elastic modulus is low, the potential for early age cracking is greatly reduced (19). In the architectural mortar reproduction, the high proportion of volcanic ash produced low temperature rise during exothermic hydration processes (51) and a slow rate of strength development. At 180 d of hydration, the inversely computed values of Young's modulus, $E = 3.37$ GPa, and modulus of rupture, $R = 1.32$ MPa, correlate well with hydrated lime mortars with ≤2-mm Pozzolane Rosse ash pozzolan in a different testing system at 180 d of hydration with 13 MPa uniaxial compressive strength (Table 1) (16, 18). This is the early stage of mortar development that Roman builders understood, at least empirically, as they carried out the construction of the large monuments. They may have relied on the more immediate gain in load-bearing strength of the brick wall facing, composed of sectioned rectangular *bipedales* and the same Pozzolane Rosse mortar. This facing, firmly connected to the conglomeratic wall core, allowed certain architectural elements to develop an intermediate cohesion that would sustain overlying structural loads (2).

The conglomeratic architectural concrete contains about 45–55 vol % coarse *caementa*, as Tufo Lionato and Tufo Giallo della Via Tiberina tuff and broken brick (16, 52). In conglomeratic rocks, about 50 vol % coarse particles creates a clast-supported framework, with large clasts touching one another in 3D space and matrix materials filling interstitices (53). Triaxial tests of experimental conglomerates show that peak stress increases with strength and stiffness of the larger clasts (54). The conglomeratic fabric of *caementa*, with its own pozzolanic properties, may provide reinforcement through a similar clast-supported framework (Fig. 1*B*) that supports tensile stresses on the order of 1 MPa in cross and barrel vaults, as in the Great Hall (11), and blunts the propagation of potentially catastrophic structural scale cracks through producing larger bridging offsets (Fig. 1*C*).

Implications

The capacity of the Roman pyroclastic aggregate concretes to crack at the macro scale but remain intact at the structural scale results from the long-term interaction between architectural form and the material response of the mortar to static loads and seismic ground shaking. The builders of Trajan's Markets were surely aware of previous ground motions that caused collapse of buildings in the city. In 15 CE, "violent earthquakes … shook down a portion of the city wall" (Cassio Dio, *Historia Romana*, 57.14.7), and in 50 CE, "houses were overturned by repeated shocks of earthquake (*crebris terrae motibus*) and, as panic spread, the weak were trampled underfoot in the trepidation of the crowd" [Tacitus, *Annals*, 12 (43)] (4, 55, 56). Roman builders constructed a series of lateral arches that connect the 8.6-m span of the central vault of the Great Hall to the surrounding superstructure (Fig. 1*A*); the elevated location of the arches was perhaps intended to mitigate both static and seismic loadings (11). Their selections of pyroclastic volcanic rock, as granular silt- to gravel-sized Pozzolane Rosse ash and as cobble-sized tuff (and brick) rubble *caementa*, played key roles in the toughening mechanisms that reinforce the durability of that concrete. The intial pozzolanic reactivity of the ash constituents—glassy alkali-rich groundmass scoriae and clay and zeolite surface textures—with portlandite was replaced by authigenic hydration processes in the presence of moisture permeating the concrete fabric that produced further crystalline cementitious reinforcements over the long-term history of the monument. Authigenic cementitious processes also occur in seawater concretes of Roman maritime harbor structures that use *pulvis*, pumiceous ash from the Gulf of Naples (*de Architectura* 2.7.2–3; 2.6.1–4) (14), but these are dominated by an Al-tobermorite and zeolite mineral assemblage (57).

An Imperial Roman concrete prototype, with pyroclastic rock as both mortar pozzolan and conglomeratic coarse aggregate, would potentially add fracture toughness and self-healing properties to specialty sealing materials (58) and constructions in areas of moderate seismic activity. Variations in the mineralogical, granulometric, and chemical compositions of a given pyroclastic deposit would have to be thoroughly understood, however, before it could satisfy quality control specifications for stability and safety considerations in modern applications. Chemical additives could enhance reactivity to promote intergrowths of platey strätlingite crystals in interfacial zones and present obstructions to crack linkages at the micrometer scale. A moderate strength would be balanced by elevated fracture toughness, service life, and resistance to chemical attack.

Materials and Methods

The Sovrintendenza Capitolina Beni Culturali di Roma Capitale provided drill cores of Markets of Trajan concretes. Mortar reproductions use a volumetric 3:1 volcanic ash–lime mix (*de Architectura* 2.5.1), with 10 wt % quicklime and water content 0.35 (51). Quicklime with ∼96 wt % CaO, similar to Roman lime calcined from Monte Soratte limestone (59), was provided by Carmeuse Lime and Stone and hydrated in a 1:1.5 ratio with Ithaca, New York tap water. The mortar was cured in 20-cm-diameter sealed plastic molds and sawed into 7.5-cm-thick arc-shaped specimens. Fracture experiments used a stiff, servo-hydraulically controlled testing apparatus, with eight tests in each chronological group. The load was applied at the top of the arc and controlled by crack mouth opening displacement (CMOD). Fracture energy (G_F) was computed via a finite element analysis (FEA) model (18) (Fig. 4 *E* and *F*). Computed tomography scans were performed at Cornell University Hospital for Animals, at "bone density" setting with 0.5-mm slice spacing. We used the ImageJ paintbrush tool to visually trace all apparent crack surfaces in the ∼75 slices of each specimen, and a crack area algorithm summed the voxels (3D pixels) of these surfaces (Fig. 4 and Fig. S2), giving a more detailed representation of crack surface area than standard methods (60). The uncertainty in crack area is ± 4% based on three independent tracings of the same specimen. The experimentally determined fracture energy (G_f) is computed by dividing the measured work of fracture, obtained by integrating experimental load vs. load-line displacement measurements, by the mapped crack surface areas (Fig. 4*E* and Fig. S2). Propagating the error in these measurements gives total error <5%. The tracings do not capture all microcracking phenomena and some

ENGINEERING

size dependence of fracture energy is expected given the quasi-brittle nature of fracture (61). Mineral compositions of the <74-μm fraction of the cementitious matrix and volcanic ash mix were evaluated with powder X-ray diffraction immediately after testing (Fig. S3). Major oxide compositions of the same fractions were obtained with high-resolution inductively coupled plasma mass spectrometry (Fig. 2*D* and Table S5). SEM energy dispersive spectral analyses (SEM-EDS) on back-scattered images (BSE) used 15-keV beam energy, 850-pA beam current, and 10-s counting time with 3,500 counts per second. Counts were converted to semiquantitative concentrations and atomic ratios for Ca, Si, and Al (Table S4). X-ray microdiffraction of crystalline phases (Fig. 3 and Table S3) in the 11MTC1 sample and the 180-02 sample, refrigerated at 36 °C in ethanol from 2010 to 2013, were determined at beamline 12.3.2 of the Advanced Light Source at Lawrence Berkeley National Laboratory. A monochromatic X-ray beam of 10 keV was focused to 2- (v) × 8- (h) μm diameter on a thin (0.3-mm) mortar slice placed in transmission mode into the beam, with the detector 2θ at 39° for sample 11MTC1 and at 360° for sample 180-02. A Pilatus 1M area detector placed at 360-mm recorded Debye rings diffracted by crystalline phases radially integrated into intensity vs. 2θ plots over an arch segment of 76° for 2θ 3°–30°.

ACKNOWLEDGMENTS. We thank Tim Bond at the Winter laboratory at Cornell University; Nathan Dykes at Cornell University Hospital for Animals; Kevin Smith, Mike Schrock, Carl Laird, and Dale Andrews at Carmeuse Lime and Stone; and Renato Perucchio, Nobumichi Tamura, Timothy Teague, Cagla Meral, John P. Oleson, Claudia Ostertag, Nichole Wonderling, Isaac Arabadjis, Laurie Hamilton, Audrey Landis, Katrina Martin, Bronze Black, and Carol Hagen for research support. This research was supported by the Loeb Classical Library Foundation at Harvard University and National Science Foundation SusCHEM Grant 1410557. Data acquired at beamline 12.3.2 at the Advanced Light Source at the Lawrence Berkeley Laboratories were supported by the Director of the Office of Science, Department of Energy, under Contract DE-AC02-05CH11231.

1. Vitti M (2007) Mercati di Traiano. *Il Museo dei Fori Imperiali nei Mercati di Traiano*, ed Ungaro L (Electra, Milan), pp 5–19.
2. Vitti M, Vitti P, *Experimental Innovations in Vaulting Construction Under Trajan and Hadrian, The Trajanic Building Programme at Rome and Its Ports*, eds Keay S, Triantafillou C (Highfield, Oxford).
3. Frepoli A, et al. (2010) Seismicity, seismogenic structures, and crustal stress fields in the greater Rome area (central Italy). *J Geophys Res* 115:B12303.
4. Galli PAC, Molin D (2013) Beyond the damage threshold: The historic earthquakes of Rome. *Bull Earthquake Eng* 10(6):1–32.
5. Aldrete GS (2007) *Floods of the Tiber in Ancient Rome* (Johns Hopkins, Baltimore).
6. Funiciello R, Lombardi L, Marra F, Parotto M (1995) Seismic damage and geological heterogeneity in Rome's colosseum area: Are they related? *Ann Geofis* 38:927–937.
7. Samuelli Ferretti A (2005) The structures of the basilica. *The Basilica of Maxentius, the Monument, Its Materials, Construction, and Stability*, ed Giavarini C (L'Erma di Bretschneider, Rome), pp 161–257.
8. Jackson MD, Deocampo D, Marra F, Scheetz B (2010) Mid-Pleistocene volcanic ash in ancient Roman concretes. *Geoarchaeology* 25(1):36–74.
9. Massazza F (1998) Pozzolana and pozzolanic cements. *Lea's Chemistry of Cement and Concrete*, ed Hewlitt P (Arnold, London), 4th Ed, pp 471–632.
10. Jackson MD, et al. (2011) Building materials of the Theater of Marcellus, Rome. *Archaeometry* 53(4):728–742.
11. Brune P, Perucchio R (2012) Roman concrete vaulting in the Great Hall of Trajan's Markets: Structural evaluation. *J Archit Eng* 18(4):332–340.
12. Marra F, et al. (2009) Large mafic eruptions at the Alban Hills Volcanic District (Central Italy): Chronostratigraphy, petrography and eruptive behavior. *J Volcanol Geotherm Res* 179:217–232.
13. Trigila R, et al. (1995) Petrology. *The Volcano of the Alban Hills*, ed Trigila R (Tipografia S.G.S., Rome), pp 95–165.
14. Granger F (1931, reprint 2002) *Vitruvius on Architecture, Books 1–5* (Loeb Classical Library Nos. 251, 280, Cambridge, UK).
15. Hillerborg A (1985) Results of three comparative test series for determining the fracture energy g_f of concrete. *Mater Struct* 18:407–413.
16. Samuelli Ferretti A (1995) Proposte per lo studio teorico-sperimentale della statica dei monumenti in opus caementicium. *Materiali e Strutture* 7:63–83.
17. Jackson MD, et al. (2009) Assessment of material characteristics of ancient concretes, Grande Aula, Markets of Trajan, Rome. *J Arch Science* 36:2481–2492.
18. Brune P, Ingraffea AR, Jackson MD, Perucchio R (2013) The fracture toughness of an imperial Roman mortar. *Eng Fract Mech* 102:65–76.
19. Metha PK, Langley WS (2000) Monolith foundation, built to last '1000 years'. *Concr Int* 7:27–32.
20. Lothenbach B, Scrivener K, Hooton RD (2011) Supplementary cementitious materials. *Cement Concr Res* 41:217–219.
21. Snellings R, Mertens G, Elsen J (2012) Supplementary cementitious materials. *Rev Mineral Geochem* 74:211–278.
22. Mills SJ, Christy AG, Genin J-MR, Kameda T, Colombo F (2012) Nomenclature of the hydrotalcite supergroup: Natural layered double hydroxides. *Min Mag (Lond)* 76(5): 1289–1336.
23. Rinaldi R, Sacerdoti M, Passaglia E (1990) Strätlingite: Crystal structure, chemistry, and a reexamination of its polytpye vertumnite. *Eur J Mineral* 2:841–849.
24. MacDowell JF (1991) Strätlingite and hydrogarnet from calcium aluminosilicate glass cements. *Proc MRS* 179:159–179.
25. Swainson IP, Dove MT, Schmahl WW, Putnis A (1992) Neutron powder diffraction study of the åkermanite-gehlenite soild solution series. *Phys Chem Minerals* 19:185–195.
26. Ben Haha M, Lothenbach B, Le Saout G, Winnefield F (2012) Influence of slag chemistry on the hydration of alkali-activated blast-furnace slag – Part II: Effect of alumina. *Cement Concr Res* 42:74–83.
27. Kwan S, LaRosa J, Grutzeck MW (1995) ^{29}Si and ^{27}Al MASNMR study of strätlingite. *J Am Ceram Soc* 78(7):1921–1926.
28. Ding J, Fu Y, Beaudoin JJ (1995) Strätlingite formation in high alumina cement-zeolite systems. *Adv Cement Res* 7(28):171–178.
29. Signoretti E, et al. (2008) I minerali della cava di Campomorto in localitá pietra massa, Montalto di Castro (VT). *Il Cercapietre* 1–2:5–33.
30. Bažant ZP, Le J-L, Bazant MZ (2009) Scaling of strength and lifetime probability distributions of quasibrittle structures based on atomistic fracture mechanics. *Proc Natl Acad Sci USA* 106(28):11484–11489.
31. van Mier JGM (1997) *Fracture Processes of Concrete* (CRC, New York).
32. Bažant ZP, Planas J (1998) *Fracture and Size Effect in Concrete and Other Quasibrittle Materials* (CRC, New York).
33. Sarkar PK, Haque R, Ramgolan KV (2013) Fracture behavior of heat cured fly ash based geopolymer concrete. *Mater Des* 44:560–568.
34. Hajimohammadi A, Provis JL, van Deventer JSJ (2010) Effect of alumina release rate on the mechanism of geopolymer gel formation. *Chem Mater* 22:5199–5208.
35. Hajimohammadi A, Provis JL, van Deventer JSJ (2011) The effect of silica availability on the mechanism of geopolymerisation. *Cement Concr Res* 41:210–216.
36. Favier A, Habert G, d'Espinose de Lacaillerie JB, Roussel N (2013) Mechanical properties and compositional heterogeneities of fresh geopolymer pastes. *Cement Concr Res* 48:9–16.
37. Hong S-Y, Glasser FP (2002) Alkali sorption by C-S-H and C-A-S-H gels Part II. Role of alumina. *Cement Concr Res* 32:1101–1111.
38. Davidovits J (2008) *Geopolymer Chemistry and Applications* (Geopolymer Institute, Saint-Quentin, France).
39. Mindess S, Diamond S (1982) The cracking and fracture of mortar. *Matériaux et Construction* 15:107–113.
40. Ostertag C, Yi CK (2007) Crack/fiber interaction and crack growth resistance behavior in microfiber reinforced mortar specimens. *Mater Struct* 40:679–691.
41. Hernández-Cruz D (2014) Multiscale characterization of chemical-mechanical interactions between polymer fibers and cementitious matrix. *Cement Concr Compos* 48: 9–18.
42. Feng QL, Lachowski EE, Glasser FP (1988) Densification and migration of ions in blast furnace slag-portland cement pastes. *Proc MRS* 136:263–272.
43. Liborio JBL, da Silva J, de Melo AB (2002) SEM analysis of the paste-aggregate interface in concrete containing silica fume. *ACI Special Publication SP207-16* (Am Concrete Inst, Farmington Hills, MI), pp 245–262.
44. Matschei T, Lothenbach B, Glasser FP (2007) The role of calcium carbonate in cement hydration. *Cement Concr Res* 37:551–558.
45. Landis EN, Bolander JE (2009) Explicit representation of physical processes in concrete fracture. *J Phys D Appl Phys* 42:214002.
46. Shah SP, Choi S (1999) Nondestructive techniques for studying fracture processes in concrete. *Int J Fract* 98:351–359.
47. Oh JE, Clark SM, Monteiro PJM (2011) Does the Al substitution in C-S-H(I) change its mechanical property? *Cement Concr Res* 41:102–106.
48. Moon J, et al. (2012) Pressure induced reactions amongst calcium aluminate phases. *Cement Concr Res* 41:571–578.
49. Yilmaz VT, Glasser FP (1992) Effect of silica fume addition on the durability of alkali-glass fibre in cement matrices. *ACI Special Publication SP132-62* (Am Concrete Inst, Farmington Hills, MI), pp 1151–1166.
50. Yi CK, Ostertag C (2005) Mechanical approach in mitigating alkali-silica reaction. *Cement Concr Res* 35:67–75.
51. Brune P (2011) The mechanics of Imperial Roman concrete and the structural design of the vaulted monuments. PhD dissertation (Univ of Rochester, Rochester, NY).
52. Jackson MD, et al. (2005) The judicious selection and preservation of tuff and travertine building stone in ancient Rome. *Archaeometry* 47(3):485–510.
53. Boggs S (2009) *Petrology of Sedimentary Rocks* (Cambridge Univ Press, Cambridge, UK), 2nd Ed.
54. Sonmez H, et al. (2006) Estimating the uniaxial compressive strength of a volcanic bimrock. *Int J Rock Mech Min Sci* 43:554–561.
55. Cary E, Foster HB (1924) *Dio Cassius: Roman History, Books 56-60* (Loeb Classical Library No. 175, Cambridge, UK).
56. Jackson J (1937) *Tacitus: Annals 13-16* (Loeb Classical Library No. 322, Cambridge, UK).
57. Jackson MD, et al. (2013) Material and elastic properties of Al-tobermorite in ancient Roman seawater concrete. *J Am Ceram Soc* 96(8):2598–2606.
58. Langton C, Roy D (1984) Longevity of bore-hole and shaft sealing materials: Characterization of ancient cement based building materials. *Mat Rec Soc Symp Proc* 26: 543-549.
59. Jackson MD, et al. (2007) Geological observations of excavated sand (*harenae fossiciae*) used as fine aggregate in ancient Roman pozzolanic mortars. *J Roman Arch* 20:1–30.
60. RILEM (1985) Determination of the fracture energy of mortar and concrete by means of three-point bend tests on notched beams. *Mater Struct* 18(106):285–290.
61. Bažant ZP (2004) Scaling theory for quasibrittle structural failure. *Proc Natl Acad Sci USA* 101(37):13400–13407.

Supporting Information

Jackson et al. 10.1073/pnas.1417456111

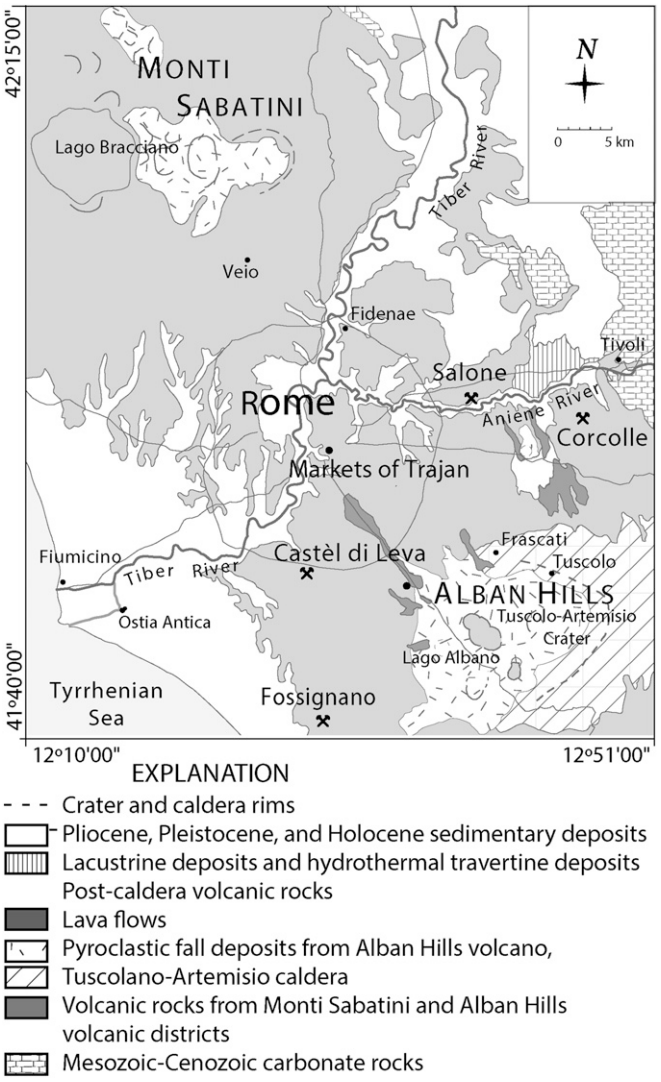

Fig. S1. Geologic sketch map of the Roman region, showing the Pozzolane Rosse quarries at Castel di Leva, Corcolle and Fossignano and Tufo Lionato quarry at Salone (after ref. 1).

1. Jackson MD, Deocampo D, Marra F, Scheetz B (2010) Mid-Pleistocene volcanic ash in ancient Roman concretes. *Geoarchaeology* 25(1):36–74.

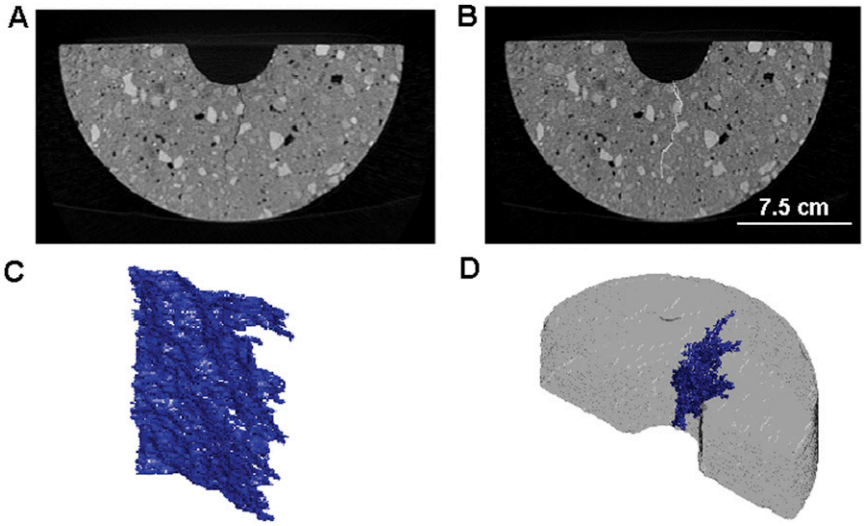

Fig. S2. Illustration of method used to determine the experimental fracture energy (G_f) from tomographic measurements. The work of fracture is obtained from the integrated load vs. load-line displacement curve and then normalized by the traced area of the tomographic fracture surfaces (Table S2). (*A*) Typical tomographic slice of a fractured specimen with the crack traced in (*B*). (*C*) Three-dimensional rendering of the complete traced crack array and (*D*) distribution of cracks in the arc-shaped mortar specimen.

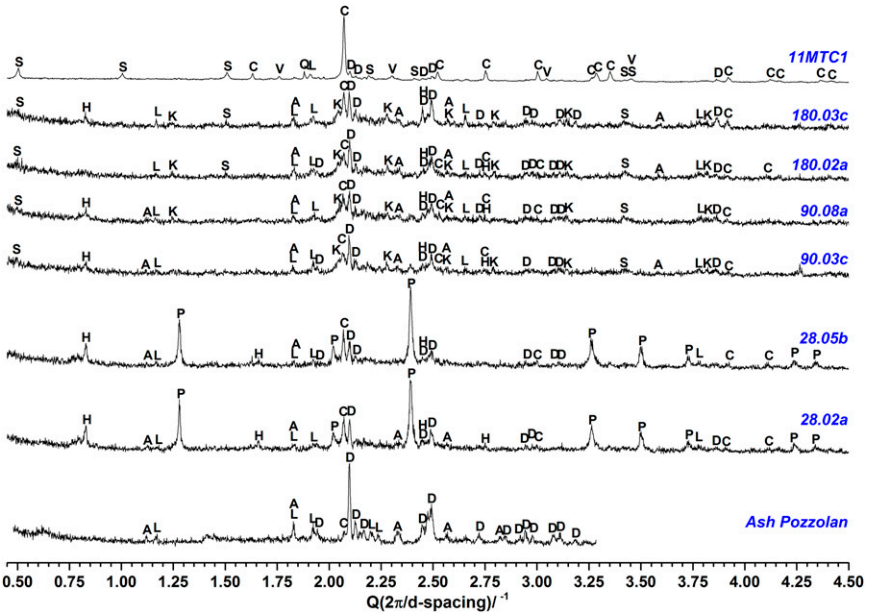

Fig. S3. Powder X-ray diffraction analyses of the cementitious matrix (<74 μm) gently tapped and hand-shaken through sieves to <200 mesh from the mortar reproduction at 28, 90, and 180 d of hydration, the 11MTC1 mortar from the foundation of the Markets of Trajan at Via Biberati and the ash pozzolan mix, using a Scintag PADV X-ray diffractometer, equipped with a Ge solid state detector and Cu–Ka radiation, 35 kV/30 mA, at the Materials Characterization Laboratory at Pennsylvania State University. For bulk chemical analyses as weight percent oxides see Table S5.

Table S1. Grain size distribution of Pozzolane Rosse ash from Castel di Leva quarry (Fig. S1), expressed as weight percent retained on sieves

	Gravel (lapilli)		Sand (ash)					Silt
ASTM sieve no.	4	8	16	30	50	100	200	PAN
Weight %	26.7	18.75	15.34	10.8	9.66	9.66	6.25	2.84
Opening size, mm	4.75	2.38	1.2	0.6	0.3	0.15	0.08	<0.075

Determined through the ASTM C36-06 Standard Test Method for Sieve Analysis of Fine and Coarse Aggregates (after ref. 1).

1. Jackson MD, et al. (2007) Geological observations of excavated sand (*harenae fossiciae*) used as fine aggregate in ancient Roman pozzolanic mortars. *J Roman Arch* 20:1–30.

Table S2. Measurements of fracture surface area in the mortar reproductions (Fig. 4)

Tomographic analysis			Experimental testing data		
Crack surfaces,* voxels	Voxel face area, mm^2	Traced crack area,† mm^2	Work of fracture (from load-loadline displacement), mJ	Experimental fracture energy (G_f), J/m^2	Peak load (P_{max}), N
113,000	0.21	11,770.01	44	4	345
85,000	0.20	8,320.96	45	5	298
120,000	0.20	11,898.16	47	4	336
67,000	0.19	6,367.54	33	5	277
120,000	0.20	11,434.29	40	3	337
110,000	0.22	12,407.43	42	3	355
—	—	—	52	—	345
—	—	—	66	—	376
55,000	0.31	8,555.95	297	35	1,986
57,000	0.30	8,579.21	319	37	1,705
50,000	0.33	8,000.67	296	37	1,740
33,000	0.31	5,154.65	342	66	2,201
44,000	0.30	6,612.96	341	52	1,833
40,000	0.20	5,890.61	263	45	1,722
44,000	0.30	6,824.25	354	52	1,703
30,000	0.30	4,767.35	299	63	1,676

Measured from computed tomography scans performed at the Cornell University Hospital for Animals, at "bone density" setting with a slice spacing of 0.5 mm, and ImageJ tracings of all apparent crack surfaces in the ~75 slices of each specimen. A crack area algorithm summed the voxels (3D pixels) of these surfaces. Dashes indicate that high-resolution scans are not available for these samples.

*Error is <5% based on tracings by as many as three different individuals.

†The traced area is the average of both walls of the cracks.

Table S3. Characteristic d-spacings of minerals identified through X-ray microdiffraction analysis (Fig. 3)

Crystallographic parameters			X-ray microdiffraction analysis		
d-spacing, Å	Intensity, %	(hkl)	180d CM Pt 11 (Fig. 3*A*)	MT CM Pt 10 (Fig. 3*C*)	MT SCOR1 Pt 18 (Fig. 3*E*)
12.59	100	0 0 3	12.62	12.40	12.51
4.20	56	0 0 9	4.22		4.20
2.87	44	1 1 0	2.87	2.87	2.87
6.30	31	0 0 6	6.29	6.27	6.30
2.61	23	1 1 6	2.61	2.61	2.61
4.16	21	1 0 5	4.16	4.17	
1.89	17	1 1 15		1.88	
		2 0 13			
1.83	16	2 0 14		1.83	1.83
4.40	15	1 0 4	4.40		4.40
2.41	14	2 0 4	2.41	2.41	
4.93	13	1 0 1		4.93	
2.03	11	1 0 17	2.02	2.02	2.02
2.12	11	1 1 12	2.12	2.12	2.12
2.37	11	1 1 9		2.37	2.37
2.51	8	1 0 13	2.51		
3.42	8	1 0 8	3.44		
2.01	6	2 0 11	2.00		2.00
	Åkermanite			MT SCOR1 Pt 18 (Fig. 3*E*)	
2.87	100	2 1 1		2.87	
3.09	23	2 0 1		3.08	
1.76	22	3 1 2		1.77	
2.48	16	3 1 0		2.49	
1.85	12	3 3 0		1.84	
1.78	11	4 1 1		1.77	
	Katoite		180d CM Pt 11 (Fig. 3*A*)		MT SCOR1 Pt 18 (Fig. 3*E*)
2.77	100	4 2 0	2.77		2.76
2.01	91	1 1 6	2.00		2.00
2.26	79	5 2 1	2.27		2.25
1.65	70	6 4 2			1.65
5.05	53	1 1 2	5.05		
3.10	52	4 0 0	3.11		
1.72	48	6 4 0			1.71
2.43	31	4 3 1	2.43		
3.31	28	3 2 1	3.33		
2.53	18	2 2 4	2.53		

Analyzed at beamline 12.3.2 of the Advanced Light Source at Lawrence Berkeley National Laboratory. A monochromatic X-ray beam of 10 keV was focused to 2- (v) × 8- (h) μm diameter on a thin (0.3-mm) slice of mortar placed in transmission mode into the beam, with the detector 2θ at 39° for the 11MTC1 sample and at 360° for the 180-02 sample. A Pilatus 1M area detector placed at 360 mm recorded Debye rings diffracted by crystalline phases that were radially integrated into intensity vs. 2θ plots over an arch segment of 76° for 2θ 3°–30°.

Table S4. Compositions of cementitious hydrates determined through SEM-EDS analyses from the 28-d (28-05), 180-d (180-02), and 1,900-y Great Hall (GRAULA20-A) mortars (Fig. 2)

Mortar, atomic %	Ca	Al	Si	Al/(Si+Al)	Ca/(Si+Al)	Ca/Si
28-d cementitious matrix						
C-A-S-H						
3.2	20.37	26.05	53.58	0.33	0.26	0.38
1.5	52.23	10.01	37.76	0.21	1.09	1.38
1.6	54.06	7.89	38.06	0.17	1.18	1.42
3.4	75.81	7.74	16.45	0.32	3.13	4.61
3.5	76.71	5.24	18.05	0.22	3.29	4.25
Fiber						
1.2	58.87	37.65	3.47	0.92	1.43	16.96
3.6	59.56	34.48	5.96	0.85	1.47	10.00
1.3	59.57	32.92	7.50	0.81	1.47	7.94
C-S-H and opal						
1.7	11.01	9.02	79.97	0.10	0.12	0.14
3.7	0.00	0.00	100.00	0.00	0.00	0.00
3.8	62.07	0.00	37.93	0.00	1.64	1.64
180-d cementitious matrix						
C-A-S-H						
4.4	47.14	10.55	42.32	0.20	0.89	1.11
4.5	47.01	14.66	38.34	0.28	0.89	1.23
5.3	46.37	12.18	41.45	0.23	0.86	1.12
5.4	47.88	17.07	35.05	0.33	0.92	1.37
3.3	41.63	14.57	43.80	0.25	0.71	0.95
1.3	44.05	13.38	42.57	0.24	0.79	1.03
15	53.51	11.95	34.54	0.26	1.15	1.55
16	45.10	11.73	43.17	0.21	0.82	1.04
17	46.63	10.22	43.15	0.19	0.87	1.08
18	46.97	11.29	41.74	0.21	0.89	1.13
19	48.48	9.29	42.23	0.18	0.94	1.15
Plate/fiber						
2.1	48.39	31.09	20.52	0.60	0.94	2.36
2.2	45.98	33.68	20.34	0.62	0.85	2.26
4.1	60.01	34.57	5.42	0.86	1.50	11.08
4.3	53.32	27.12	19.57	0.58	1.14	2.72
6.4	59.73	38.18	2.10	0.95	1.48	28.46
Al-rich C-A-S-H						
3.1	52.75	38.51	8.74	0.81	1.12	6.03
4.2	52.33	38.08	9.59	0.80	1.10	5.45
5.1	54.34	36.96	8.70	0.81	1.19	6.24
5.2	52.22	39.81	7.96	0.83	1.09	6.56
6.1	45.13	38.18	16.69	0.70	0.82	2.70
6.2	44.42	26.76	28.82	0.48	0.80	1.54
6.3	46.13	30.28	23.58	0.56	0.86	1.96
6.5	44.78	33.52	21.70	0.61	0.81	2.06
Great Hall, cementitious matrix						
C-A-S-H						
1	59.68	24.10	16.23	0.60	1.48	3.68
2	42.76	34.36	22.88	0.60	0.75	1.87
3	40.82	33.15	26.03	0.56	0.69	1.57
5	32.23	38.34	29.43	0.57	0.48	1.10
7	31.81	38.32	29.86	0.56	0.47	1.07
14	40.46	32.90	26.64	0.55	0.68	1.52
17	24.64	41.76	33.60	0.55	0.33	0.73
18	31.70	31.86	36.44	0.47	0.46	0.87

Analyzed using a Zeiss EVOMA10 scanning electron microscope at the Department of Earth and Planetary Science at the University of California, Berkeley. Operating conditions were a beam energy of 15 keV, beam current of 850 pA, and counting time of 10 s with 3,500 counts per second for EDS analyses. Counts were converted to semiquantitative concentrations and atomic ratios for Ca, Si, and Al.

Table S5. Major element compositions as weight percent oxides of the <74 μm fraction (passing the 200 sieve) of the ash pozzolan and mortars

Sample	SiO_2	Al_2O_3	Fe_2O_3(T)	MnO	MgO	CaO	Na_2O	K_2O	TiO_2	P_2O_5	LOI	Total
Ash Pozzolan												
01	43.48	16.58	9.46	0.18	3.72	10.10	0.80	2.45	0.80	0.67	10.90	99.14
02	43.80	16.73	9.40	0.18	3.73	9.89	0.82	2.50	0.80	0.65	11.23	99.72
28 d												
28.02a	19.76	8.00	3.98	0.09	1.90	32.28	0.32	1.15	0.34	0.27	28.50	96.57
28.05b	18.08	7.43	3.56	0.08	1.73	33.31	0.28	0.97	0.30	0.22	30.94	96.89
28.05c	20.06	8.08	3.96	0.09	1.88	31.18	0.33	1.18	0.34	0.25	27.11	94.46
90 d												
90.08a	22.35	8.71	4.42	0.09	2.00	23.88	0.34	1.17	0.38	0.29	30.98	94.61
90.08b	22.46	8.91	4.26	0.09	1.94	24.71	0.32	1.13	0.36	0.27	31.23	95.70
90.03c	21.83	8.49	4.23	0.09	1.92	24.71	0.30	1.14	0.36	0.28	33.95	97.29
180 d												
180.02a	23.07	9.07	4.34	0.10	1.97	22.94	0.33	1.22	0.37	0.30	33.33	97.02
180.02b	21.74	8.62	4.04	0.09	1.80	21.46	0.33	1.14	0.34	0.26	36.80	96.63
180.03c	22.44	9.02	4.25	0.09	1.90	23.10	0.31	1.16	0.36	0.27	36.42	99.32
1,900 y												
11MTC1	24.49	9.43	2.65	0.06	1.53	28.14	0.61	0.98	0.24	0.22	30.69	99.04

The compositions of the Trajanic volcanic ash mix, mortar reproduction at 28, 90, and 180 d of hydration and the 11MTC1 mortar specimen from the foundation of the Markets of Trajan at Via Biberati (Fig. 2*E*), were determined through lithium metaborate/tetraborate fusion with high-resolution inductively coupled plasma mass spectrometry, at Activation Laboratories, Ontario, Canada. For X-ray powder diffraction studies see Fig. S3.